12th International Symposium on Turbulence and Shear Flow Phenomena (TSFP12)
Osaka, Japan, July 19–22, 2022

SPECTRAL PROPER ORTHOGONAL DECOMPOSITION FOR COUPLED HYDRODYNAMIC/ACOUSTIC FIELDS

Maxime Fiore, Hélène Parisot-Dupuis, Benjamin Etchebarne and Romain Gojon
Department of aerodynamics and Propulsion (DAEP)
ISAE-SUPAERO, University of Toulouse
10 Avenue Édouard Belin, 31400 Toulouse, France
*email: romain.gojon@isae-supaero.fr

ABSTRACT

In a large number of flow configurations, the complexity of the phenomena involved and their potential interaction can make the analysis of the flow field difficult. In the purpose to decompose the flow in distinct and simpler phenomena, the proper orthogonal decomposition (POD) has been developed and make possible to isolate different phenomena and sort them in decreasing order of magnitude based on a metric chosen *a priori*. Recently, the spectral POD (SPOD) has been developed by adding a preceding discrete Fourier transform (DFT) step which allows to have the frequency information on the modes retrieved by the POD. This gives the possibility to isolate several phenomena occurring at a same frequency. Based on the theoretical background proposed by Schmidt *et al.*, this method has been widely validated in hydrodynamic configurations showing its good behavior compared to other modal decomposition methods, namely DFT or dynamical mode decomposition (DMD). However, in flow configurations where both the hydrodynamic and acoustic fields interact, without additional treatment, the hydrodynamic field is generally dominant and only the hydrodynamic modes emerge. Furthermore, the transfer function between the hydrodynamic (source) field and the resulting acoustic (propagating) field is generally case dependant, making difficult to propose a weighting/normalization adapted for all aero-acoustic configurations. This paper proposes a general framework based on some pre-processing steps on the input aero-acoustic fields to make the hydrodynamic and acoustic fields of comparable magnitude for the SPOD. The purpose is then to analyze how the hydrodynamic field leads to the acoustic field and the possible feedback effect. This framework is illustrated on a supersonic impinging jet flow configuration used as an input data for the SPOD, and based on wall-resolved compressible large-eddy simulations (LES) where both the hydrodynamic and acoustic fields are solved.

INTRODUCTION

The analysis of the aero-acoustic field in flow configurations is generally made difficult for several reasons: the acoustic field is usually induced by complex hydrodynamic phenomena; several hydrodynamic/acoustic phenomena can coexist with some difficulty to separate their contributions. The latter issue has been investigated in the context of turbulent flow by Lumley (1981). The authors proposed to apply the proper orthogonal decomposition (POD) to the data obtained from a turbulent flow in order to decompose the complex field in simpler structures (defined as the ones with largest probability to occur in the turbulent flow) and sorted them in decreasing magnitude according to a norm defined *a priori*, the energy contained in each mode for example. More recently, a preceding step corresponding to a discrete Fourier transform (DFT) has been added to the POD and named spectral POD (SPOD). This method presents the advantage to add up a frequency information on the different phenomena captured by the POD. This method has been described by Schmidt & Colonius (2020), the authors providing proper theoretical weighting/normalization for the field variables (density, velocity and temperature fluctuations for compressible flows) in order to capture hydrodynamic flow phenomena. When applying the SPOD treatment with such normalization to configurations where both acoustic and hydrodynamic interact, the acoustic phenomena generally do not emerge. The POD step of the algorithm could be able to separate coherent structures, namely the hydrodynamic and acoustic structures. However, the acoustic part is generally of very low energy content, corresponding to several order of magnitudes under the energy level of the hydrodynamic component in the majority of flow configurations. The POD, which is based on an energy optimal decomposition, has been tested in such kind of configuration (hydrodynamic turbulence-acoustic interaction) by Druault *et al.* (2013) and Gaudard *et al.* (2014). It was observed that the first POD modes act as a filtering technique in the wavenumber space (that contains the main part of the signal energy) but cannot properly separate both components especially in the low frequency-low wavenumber domain. Therefore, the SPOD being not able to separate the acoustic and hydrodynamic phenomena in its basic implementation, the idea could be to find a suitable normalization/weighting for the input data given to the SPOD. Two relevant flow quantities to study aero-acoustic interactions are the velocity fluctuations (carrying hydrodynamic source field) and pressure fluctuations (carrying the acoustic propagating field). However, the transfer function between hydrodynamic and acoustic fluctuations is generally case dependent and no general theoretical normalization can be derived for any aero-acoustic fields (i.e. apply a different weighting for velocity fluctuations related to hydrodynamic source and pressure fluctuations related to acoustic propgation) as the one proposed by Schmidt & Colonius (2020) for hydrodynamic fields.

This paper proposes to apply general pre-processing steps to the input data of the SPOD to make the hydrodynamic and acoustic fields of the same order of magnitudes in order to properly analyze the acoustic field with the SPOD treatment and its interactions with the source hydrodynamic field. This

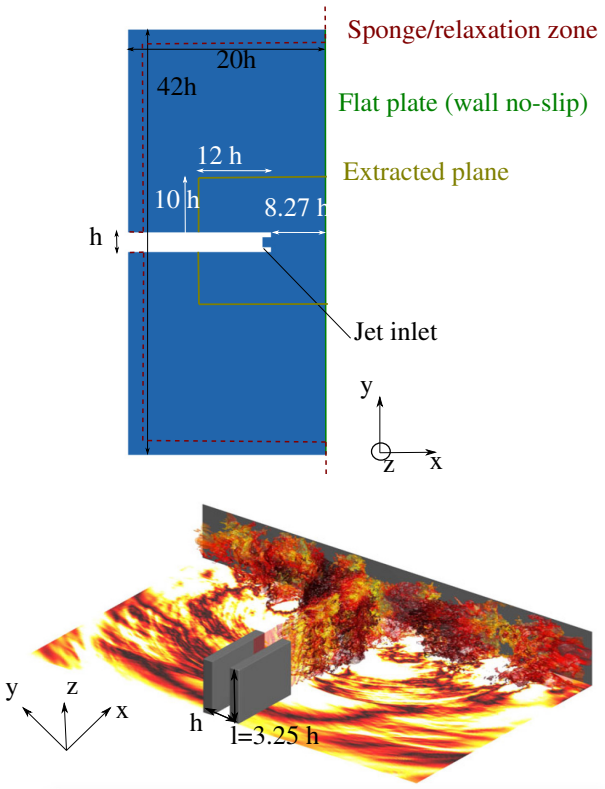

Figure 1. Simulation domain projected in the (x,y) plane (top) and iso-surfaces of density associated with 1.25 kg.m^{-3} coloured by the local Mach number, and of the pressure fluctuations in the plane (x,y) using a colour scale ranging from -7500 to 7500 Pa (bottom).

process is mainly based on two steps: the splitting of the flow field into a domain dominated by the hydrodynamic effects and a remaining domain where the acoustic field propagates; and a normalization of these two regions to have similar levels of fluctuations for the hydrodynamic and acoustic fields. The process and the analysis of this approach are illustrated on a normal impinging jet flow configuration simulated using large-eddy simulation (LES) and validated in a previous study (Gojon *et al.* (2016)).

The paper is organized as follows: Sec. 1 introduces the configuration and the numerical setup; The pre-processing steps to adapt the input fields, the SPOD algorithm and corresponding parameters used for the study are detailed in Sec. 2; the analysis of the SPOD treatment for the coupled hydrodynamic/acoustic fields is detailed in Sec. 3.

1 CONFIGURATION/NUMERICAL METHODS

A detailed description of the physics of a supersonic planar jet impinging on a flat plate normally and the corresponding numerical details for LES calculations are provided in Gojon *et al.* (2016), but a brief description is provided here. The impinging jet flow configuration shown in Fig. 1 originates from a planar straight nozzle of height $h = 0.002$ m, width $l = 3.25\ h$ in the spanwise direction, and whose lip is $0.5\ h$ thick, in an ambient medium at temperature $T_0 = 293$ K and pressure $p_0 = 10^5$ Pa. Different nozzle-to-plate distances L have been investigated ($3.94\ h$, $5.5\ h$, $8.27\ h$ and $9.1\ h$) but the present study focuses on the $8.27\ h$ case. At the nozzle exit, the jet is ideally expanded, with a

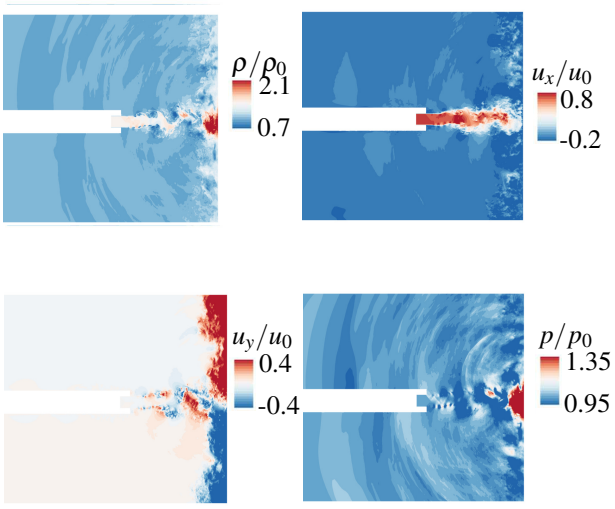

Figure 2. Instantaneous fields of density, axial (u_x), tangential (u_y) velocities and pressure in the (x,y) plane (center of the jet nozzle length ($z = l/2$)).

Mach number of $M_0 = u_0/c = 1.28$ and a Reynolds number of $Re = u_0 h/\nu = 5 \times 10^4$, where u_0, c and ν are respectively the jet velocity, the speed of sound at the nozzle exit, and the kinematic molecular viscosity (the stagnation temperature being equal to the ambient temperature). At the nozzle inlet, a Blasius laminar boundary-layer profile of thickness $0.075\ h$ and a Crocco-Busemann profile are imposed for velocity and density. The ejection conditions of the jet and the ratios between the nozzle-to-plate distances and the exit diameter in the simulations are identical to those in the experiments of Thurow *et al.* (2002). In order to generate velocity fluctuations at the nozzle exit, low-amplitude random vortical disturbances, not correlated in the spanwise direction, are added in the nozzle boundary layer at $x = -0.25\ h$ using a procedure detailed in Bogey *et al.* (2011). The forcing strength is set to $\alpha = 0.02$.

The unsteady compressible Navier-Stokes equations are solved in a cartesian coordinate system (x,y,z) by using an explicit six-stage Runge-Kutta algorithm for time integration and low-dispersion explicit eleven-point finite differences for spatial derivation (Bogey & Bailly (2004); Berland *et al.* (2007)). At the end of each time step, a sixth-order eleven-point filtering (Bogey *et al.* (2009)) is applied to the flow variables in order to remove grid-to-grid oscillations and to relax turbulent energy from scales at wave-numbers close to the grid cutoff wave-number. Thus, the filtering acts as a subgrid-scale model in the LES (Bogey & Bailly (2004, 2009); Fauconnier *et al.* (2013); Kremer & Bogey (2015)). The radiation conditions of Tam & Dong (1994) are implemented at the inflow and lateral boundaries of the computational domain. A sponge zone combining grid stretching and Laplacian filtering is also employed in order to damp the turbulent fluctuations before they reach the lateral boundaries. Adiabatic conditions are imposed at the nozzle walls and at the flat plate. A shock-capturing filtering is also applied in order to avoid Gibbs oscillations near shocks. It consists in applying a conservative second-order filter at a magnitude determined each time step using a shock sensor (Bogey *et al.* (2009)).

The simulations have been carried out using an OpenMP-based in-house solver, and a total of 200,000 iterations are computed after the transient period. The temporal discretization is equal to $\Delta t \sim 0.003 h/u$, yielding to a simulation time of $T_{sim} \sim 600\ h/u$. The mesh is composed of 250×10^6 points.

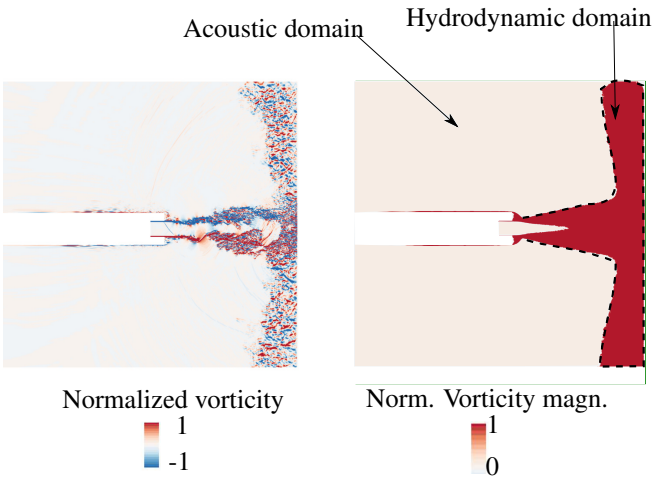

Figure 3. Instantaneous normalized vorticity field (left) and temporally averaged vorticity magnitude field (right) used to compute the threshold vorticity value.

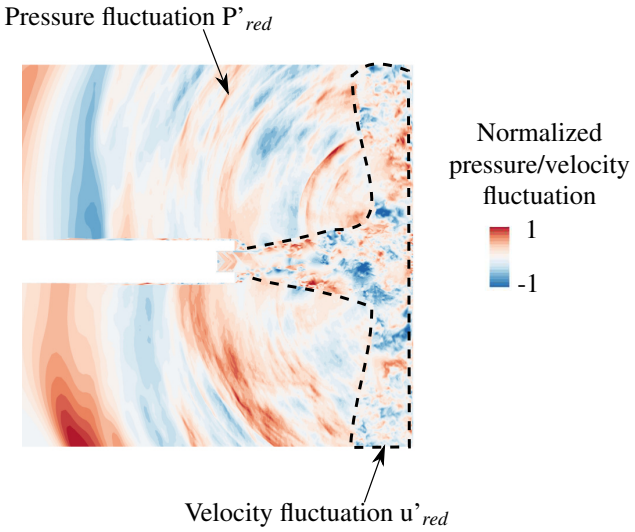

Figure 4. Instantaneous mixed normalized pressure/velocity fluctuation field (snapshot) used as an input to the SPOD.

2 PRE-PROCESSING/SPOD ALGORITHM

The input data corresponds to 4,000 two dimensional cuts snapshots sampled at the frequency St $=fh/u_0 = 6.4$ where f is the frequency, and containing the variables $[\rho,u_x,u_y,p]$ extracted from the LES simulation from Gojon *et al.* (2016) (see Fig. 2). The planes are extracted at the center of the jet nozzle length in the z direction ($z = l/2$) and the corresponding (x,y) planes are reduced in the x and y directions compared to the full simulation domain (see Fig. 1). This size domain reduction is performed in order to avoid regions in the sponge zone and have mesh sizes around the jet sufficiently fine to transport acoustic waves, the mesh being progressively coarsened as we move away from the jet. The extracted planes extends from -12 h to 8.27 h in the axial direction, the origin being the jet lip inlet. In the y direction, the mesh extends from -10 h to 10 h, the origin being the center of the jet. Based on the numerical parameters of the LES simulation (around 6 points/wavelength) and the coarser mesh size at the boundaries of the plane ($\Delta x \simeq 10h$, $\Delta y \simeq 8h$), the plane data used as an input of the SPOD can capture phenomena until St = 5.0. The spatial domain is first split into a region dominated by hydrodynamic instabilities and the remaining domain considered as the acoustic propagating domain. To do so, in each cell of the (x,y) reduced planes, the z-component of the vorticity ω_z and its modulus (vorticity magnitude) are computed along the 4,000 temporal snapshots (see Fig. 3):

$$|\omega_z| = |\frac{\partial u_y}{\partial x} - \frac{\partial u_x}{\partial y}|. \tag{1}$$

The minimum and maximum values of the vorticity magnitude in all cells and over time $|\omega_z|_{\min}$ and $|\omega_z|_{\max}$ are stored. These two quantities are then used to build a threshold for the vorticity defined as:

$$|\omega_z|_{\text{thres}} = |\omega_z|_{\min} + 0.1(|\omega_z|_{\max} - |\omega_z|_{\min}). \tag{2}$$

For each cell of the domain, if the value of the vorticity magnitude overcomes at least one time the threshold value, then this cell is tagged as being enclosed in the region dominated by hydrodynamic fluctuations. On the contrary, the un-tagged cells are considered to be in the acoustic domain. For the impinging jet, the hydrodynamic region corresponds to the jet flow, the mixing region with the fluid at rest (expansion of the jet flow) and the region close to the wall corresponding to the two wall jets created after the impact on the flat plate (see Fig. 3). It can be noticed that this "hydrodynamic" region also contains an acoustic propagation, but the velocity/pressure fluctuations associated to the acoustic waves are several order of magnitude lower than the hydrodynamic/pressure fluctuations, and these fluctuations are mixed so that separate acoustic from hydrodynamic is difficult. This is pointed out by Arndt *et al.* (1997); Tinney & Jordan (2008); Grizzi & Camussi (2012); Mancinelli *et al.* (2017) whose tried to split the fluctuations between non-radiating hydrodynamic and radiating acoustic. For the cells in the hydrodynamic region, the velocity fluctuations are considered since this variable holds the source term of hydrodynamic fluctuations. In the acoustic region, the pressure fluctuations are considered since this quantity holds the acoustic propagation. The resulting snapshots consists of mixed fields in velocity and pressure fluctuations. In order to provide similar amplitudes for these two variables, the velocity and pressure fluctuations are reduced using the global maximum, along time and in all the corresponding hydrodynamic/acoustic part of the field, of the root mean square (RMS) values of these two variables yielding to (see Fig. 4):

$$u'_{red} = \frac{u'}{u_{\text{RMS}}} \quad P'_{red} = \frac{P'}{P_{\text{RMS}}}. \tag{3}$$

u' being either the axial velocity fluctuation (u'_x) or the vertical velocity fluctuation (u'_y). The corresponding spatio-temporal matrix Q' used as an input for the SPOD can be written as:

$$Q' = \begin{pmatrix} (P'_{red})_{1,1} & (P'_{red})_{1,2} & \cdots\cdots & (P'_{red})_{1,n_{\text{snap}}} \\ (u'_{red})_{2,1} & (u'_{red})_{2,2} & \cdots\cdots & (u'_{red})_{2,n_{\text{snap}}} \\ \vdots & \vdots & \vdots\ \vdots & \vdots \\ (u'_{red})_{n_{\text{ndof}}-1,1} & (u'_{red})_{n_{\text{ndof}}-1,2} & \cdots\cdots & (u'_{red})_{n_{\text{ndof}}-1,n_{\text{snap}}} \\ (P'_{red})_{n_{\text{ndof}},1} & (P'_{red})_{n_{\text{ndof}},2} & \cdots\cdots & (P'_{red})_{n_{\text{ndof}},n_{\text{snap}}} \end{pmatrix} \tag{4}$$

where each column represents one snapshot of the full spatial plane of mixed pressure and velocity fluctuations, and a line represents the time evolution of a single spatial point and can be either pressure or velocity fluctuations time signal.

The mathematical basis of the SPOD method is detailed in Sieber *et al.* (2016) and Towne *et al.* (2018), its use is detailed in Schmidt & Colonius (2020) and applications to fluid flows is provided in Ghate *et al.* (2020) and Abreu *et al.* (2020). The SPOD method relies on the DFT and POD methods. For the present study, 4,000 snapshots (n_{snap}) of the 2D plane are used. The dataset is partitioned into smaller overlapping blocks, each of which represents an ensemble realization of the flow. It corresponds to a splitting of the initial matrix Q' into 8 blocks with 50% overlapping corresponding to 512 snapshots by block. A temporal DFT of each block is then calculated. To reduce spectral leakage, a Hanning window is used to limit the discontinuities with a hypothetical next period. The frequency resolution is around $\Delta\text{St} = 0.007$ to be compared with a frequency resolution of around 0.0015 for a classic DFT analysis. New data matrices denoted $\widehat{Q'_k}$ are formed at the k-th frequency by collecting all of the Fourier realizations of the different blocks at frequency k. The auto-covariance matrix is built for each frequency obtained with the DFT yielding to:

$$\widehat{R'_k} = W(\widehat{Q'_k})^T \widehat{Q'_k} \text{ for } k \in [1, n_{\text{dft}}] \tag{5}$$

where W is the weighting matrix representing the individual area (dA) of each cell of the spatially discretized plane:

$$W = \begin{pmatrix} dA_{1,1} & dA_{1,2} & \cdots & \cdots & dA_{1,n_{\text{snap}}} \\ \vdots & \vdots & \vdots & \vdots & \vdots \\ dA_{n_{\text{ndof}},1} & dA_{n_{\text{ndof}},2} & \cdots & \cdots & dA_{n_{\text{ndof}},n_{\text{snap}}} \end{pmatrix}. \tag{6}$$

The terms of the matrix $(\widehat{R'_k})_{k\in[1,n_{\text{dft}}]}$) correspond either to non-dimensional hydrodynamic fluctuation energy when the spatial point is in the hydrodynamic region, or to non-dimensional acoustic energy when the spatial point is in the acoustic region. The converged estimation of the cross-spectral density tensor is obtained by averaging the spectra over multiple realizations of the flow using Welch's method. The POD treatment is then applied to the matrices $(\widehat{R'_k})_{k\in[1,n_{\text{dft}}]}$ at each of the DFT frequencies. This corresponds to solve the Fredholm eigenvalue problem for each frequency k (or equivalently perform the singular value decomposition of the matrices $(\widehat{R'_k})_{k\in[1,n_{\text{dft}}]}$):

$$\int_{\mathscr{A}} R'_k \, \Phi_l(r,z)\, \mathrm{d}r\mathrm{d}z = \lambda_l \Phi_l(r,z),\ k \in [1, n_{\text{dft}}] \tag{7}$$

where (λ_l, Φ_l) are the l-th eigenvalue and eigenfunction from the singular value decomposition of the matrix $\widehat{R'_k}$ at frequency k. The eigenvalues and eigenvectors are sorted from higher to lower energy content and a fixed number n_{modes} is generally retained. The temporal functions of the POD treatment are obtained by projection of the original fluctuating field $q' \in \left[u'_{red}, P'_{red}\right]$ at a fixed frequency k onto the eigenvectors $(\Phi_l)_{l\in[1,n_{\text{modes}}]}$:

$$a_l(t) = \int_{\mathscr{A}} q'(r,z,t)\Phi_l(r,z)\mathrm{d}r\mathrm{d}z, \tag{8}$$

the families $(\Phi_l)_{l\in[1,n_{\text{modes}}]}$, $(a_l)_{l\in[1,n_{\text{modes}}]}$ being respectively orthonormal basis. The SPOD treatment provides for each variables u'_r, P'_r a set of frequencies k, eigenvectors, eigenvalues, and temporal functions for each of these frequencies $(\lambda_{k,l}, \Phi_{k,l}, a_{k,l})_{(k,l)\in[1,n_{\text{dft}}]\times[1,n_{\text{modes}}]}$.

3 SPOD ANALYSIS

The analysis of the aero-acoustic field of the impinging jet flow is split into two parts: the analysis of the hydrodynamic field in the full domain performed by using the vertical velocity field as a direct output of the LES simulation, and the mixed vertical velocity/pressure algorithm proposed in this study is used to obtain the decoupling between hydrodynamic sources and their propagation in the flow domain.

3.1 Vertical velocity field in the full domain

The eigenvalues associated to the first 5 (out of the 8) most energetic velocity fluctuation SPOD modes (vertical velocity fluctuation contribution to the turbulent kinetic energy) obtained considering the reduced-size extracted planes are shown in Fig. 5. Each eigenvalue has been non-dimensionalized by the sum of all eigenvalues for each SPOD mode and over all frequencies (total turbulent kinetic energy in the flow) to provide the relative contribution of each SPOD mode at each frequency to the vertical velocity contribution in the turbulent kinetic energy balance. The mode 1 (most energetic POD mode over all the frequency range denoted SPOD1) exhibits few main peaks. At these frequencies, the magnitude ratio with subsequent SPOD modes is relatively large (generally one order of magnitude) so that the majority of the energy at these frequencies is hold by the mode SPOD1. This observation means that, at these frequencies, only one mechanism is taking place in the flow domain. Out of these main peaks, the background level can be related to the broadband energy contribution of turbulence where the different SPOD modes have similar energy magnitudes (in general ratios between 1 and 2). The integration of all the eigenvalues of the SPOD modes over all frequencies provide the contribution of the vertical velocity fluctuation to the turbulent kinetic energy contained in the extracted plane. This same analysis led for the axial velocity fluctuation shows that the turbulent kinetic energy is generated at 47.3 % by the axial velocity fluctuation and 52.7 % by the studied vertical velocity fluctuation.

The 6 first most energetic peaks of SPOD1 for the vertical velocity fluctuation (denoted 1 to 6 in Fig. 5) are shown in Fig. 6. The first peak of SPOD1, at St = 0.092, has an anti-symmetrical footprint in the jet and in the acoustic regions with large scale coherent structures that extent in the jet region and propagating acoustic waves outside of the jet. This frequency is thus related to a symmetric oscillation mode of the jet, the jet axis being an axis of symmetry for the vertical velocity in presence of a symmetric mode. The second (St = 0.11), third (St = 0.165), fourth (St = 0.21), fifth (St = 0.24) and sixth (St = 0.29) peaks present a similar flow pattern with symmetrical structures released at the center of the jet with a size that typically represent the nozzle height. They are thus associated to an anti-symmetric oscillation mode of the jet. Finally, the dominant peak for the vertical velocity fluctuation corresponds to the peak 4 of SPOD1 at St = 0.21.

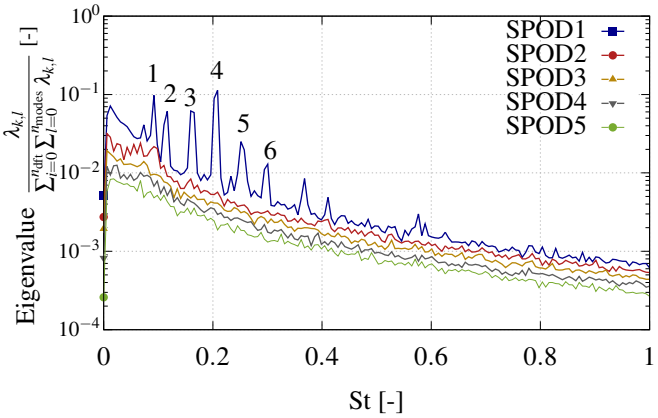

Figure 5. SPOD eigenvalues as a function of frequency (St) based on the vertical velocity fluctuations field in the full domain for the 5 most energetic SPOD modes (SPOD1 to SPOD5), logarithmic scale for the *y*-axis.

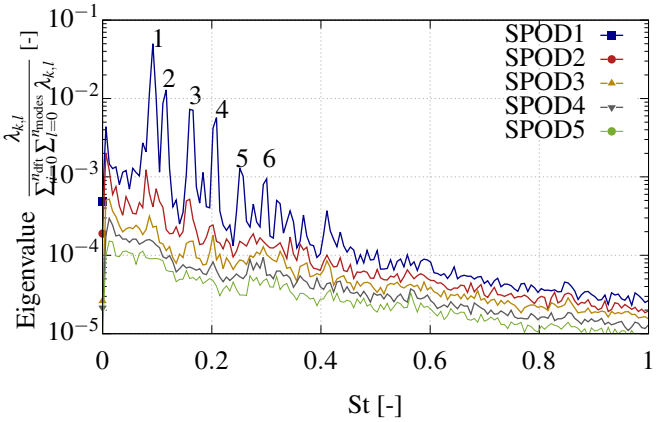

Figure 7. SPOD eigenvalues as a function of frequency (St) based on the mixed field pressure/vertical velocity fluctuations for the 5 most energetic SPOD modes (SPOD1 to SPOD5), logarithmic scale for the *y*-axis.

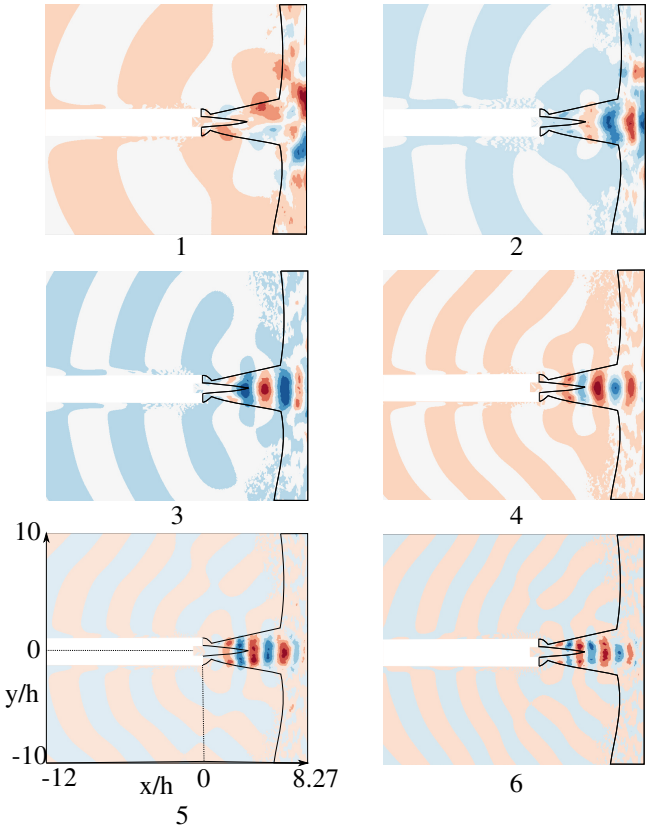

Figure 6. Vertical velocity fluctuations SPOD temporal modes in the full domain for the 6 most energetic structures of SPOD1.

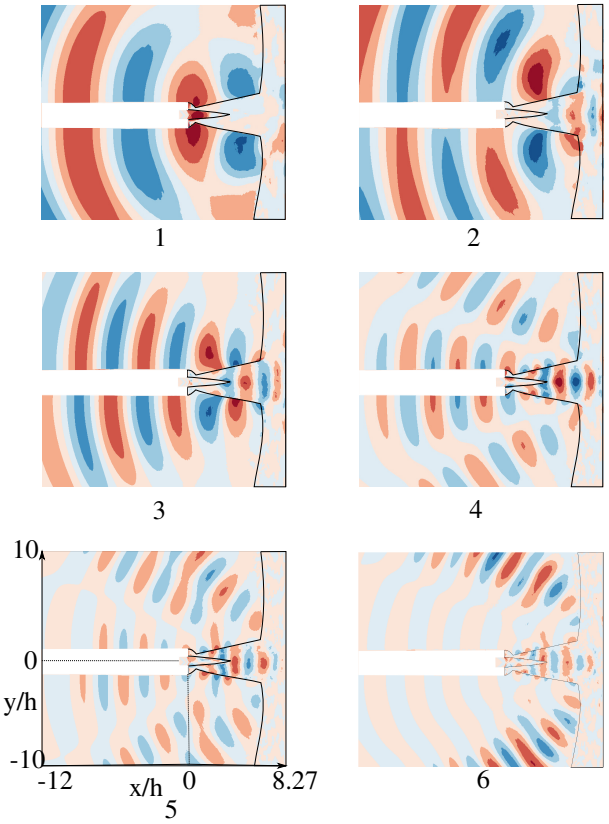

Figure 8. Mixed vertical velocity/pressure fluctuations SPOD temporal modes in the full domain for the 6 most energetic structures of SPOD1.

3.2 Mixed vertical velocity/pressure fluctuations

The first 5 most energetic mixed vertical velocity/pressure fluctuation modes (SPOD1 to SPOD5) obtained by considering the hydrodynamic (axial velocity fluctuation imposed) and acoustic domain (pressure fluctuation imposed) are shown in Fig. 7. The shape of the SPOD1 mode is strongly correlated to the shape of the mode SPOD1 for the vertical velocity alone. The corresponding 6 first most energetic peaks temporal modes of the SPOD1 are shown in Fig. 8. For the first peak of the SPOD1, almost no coherent structure of vertical velocity fluctuation can be exhibited in the hydrodynamic region that would indicate that the source of the symmetrical pattern of the pressure fluctuations in the acoustic region is mainly correlated to the axial velocity large scale structures in the jet. However, for the peaks two to six of SPOD1, coherent structures of vertical velocity fluctuations can be observed. These structures are symmetrical with respect to the main axis with correspond-

ing anti-symmetric pressure fluctuation modes in the acoustic region, as expected. For those modes, the source of the anti-symmetrical pattern of the pressure fluctuations in the acoustic region is mainly correlated to the vertical velocity large scale structures in the jet. Finally, the dominant peak for the present mixed vertical velocity/pressure fluctuation corresponds to the peak 1 of SPOD1 at St = 0.092. This tone is the main acoustic tone of the jet (Gojon *et al.* (2016)) and becomes dominant with the pre-processing steps presented in the present paper.

CONCLUSION AND PERSPECTIVES

In the purpose to isolate hydrodynamic, acoustic phenomena and their interaction when using the spectral proper orthogonal decomposition (SPOD) technique, a framework has been developed that consists in few pre-processing steps applied to the SPOD input data. This method has been used to study the aeroacoustics of a supersonic impinging jet flow field obtained from a LES simulation.

Overall, the mode 1 (most energetic POD mode over all the frequency range denoted SPOD1) exhibits few main peaks. At these frequencies, the magnitude ratio with subsequent SPOD modes is relatively large (generally one order of magnitude) so that the majority of the energy at these frequencies is hold by the mode SPOD1. This observation means that, at these frequencies, only one mechanism is taking place in the flow domain. The peaks obtained for SPOD1 are similar to the one obtained in the original study presenting theses jets and using a classic DFT algorithm. Moreover, the same oscillation modes of the jet were retrieved. It is interesting to notice that the main peak of the SPOD1 mode is not the same when using the vertical velocity or the proposed mixed velocity/pressure fluctuations field for the SPOD analysis, highlighting another aeroacoustic phenomena. In the future, more complex aeroacoustic flows will be studied in order to verify if the present methodology is capable to extract reduced order models of the flow with for each mode, its hydrodynamic and acoustic footprints, and their interactions.

ACKNOWLEDGEMENTS

This work was performed using resources from GENCI [CCRT-CINES-IDRIS] (Grant 2021-[A0102A07178]) and CALMIP (Project 1425-21A).

REFERENCES

Abreu, L. I., Cavalieri, A. V. G., Schlatter, P., Vinuesa, R. & Henningson, D. S. 2020 Spectral proper orthogonal decomposition and resolvent analysis of near-wall coherent structures in turbulent pipe flows. *Journal of Fluid Mechanics* **900** (122-144).

Arndt, R. E.A., Long, D. F. & Glauser, M. N. 1997 The proper orthogonal decomposition of pressure fluctuations surrounding a turbulent jet. *Journal of Fluid Mechanics* **340** (1), 1–33.

Berland, J, Bogey, C, Marsden, O & Bailly, C 2007 High-order, low dispersive and low dissipative explicit schemes for multiple-scale and boundary problems. *Journal of Computational Physics* **224** (2), 637–662.

Bogey, C & Bailly, C 2004 A family of low dispersive and low dissipative explicit schemes for flow and noise computations. *Journal of Computational Physics* **194** (1), 194–214.

Bogey, C. & Bailly, C. 2009 Turbulence and energy budget in a self-preserving round jet: Direct evaluation using large eddy simulation. *Journal of Fluid Mechanics* **627** (2), 129–160.

Bogey, C, de Cacqueray, N & Bailly, C 2009 A shock-capturing methodology based on adaptative spatial filtering for high-order non-linear computations. *Journal of Computational Physics* **228** (5), 1447–1465.

Bogey, C., Marsden, O. & Bailly, C. 2011 Large-eddy simulation of the flow and acoustic fields of a Reynolds number 105 subsonic jet with tripped exit boundary layers. *Physics of Fluids* **23** (3), 105–128.

Druault, P, Hekmati, A & Ricot, D 2013 Discrimination of acoustic and turbulent components from aeroacoustic wall pressure field. *Journal of Sound and Vibration* **332** (28), 7257–7278.

Fauconnier, D., Bogey, C. & Dick, E. 2013 On the performance of relaxation filtering for large-eddy simulation. *Journal of Turbulence* **14** (1), 22–49.

Gaudard, E, Druault, P, Marchiano, R & Herpe, F V 2014 About the POD application for separating acoustic and turbulent fluctuations from wall pressure synthesised field. *International Journal of Aerodynamics* **4** (1-2), 108–133.

Ghate, A. S., Towne, A. & Lele, S. K. 2020 Broadband reconstruction of inhomogeneous turbulence using spectral proper orthogonal decomposition and Gabor modes. *Journal of Fluid Mechanics* **888** (1), 111–133.

Gojon, R, Bogey, C & Marsden, O 2016 Investigation of tone generation in ideally expanded supersonic planar impinging jets using large-eddy simulation. *Journal of Fluid Mechanics* **808** (1), 90–115.

Grizzi, S. & Camussi, R. 2012 Wavelet analysis of near-field pressure fluctuations generated by a subsonic jet. *Journal of Fluid Mechanics* **698** (1), 93–124.

Kremer, F & Bogey, C 2015 Large-eddy simulation of turbulent channel flow using relaxation filtering: Resolution requirement and Reynolds number effects. *Computers and Fluids* **116** (1), 17–28.

Lumley, J. L. 1981 Coherent structures in turbulence. *Transition and turbulence* **4** (1), 215–242.

Mancinelli, M, Pagliaroli, T, Di Marco, A, Camussi, R & Castelain, T 2017 Wavelet decomposition of hydrodynamic and acoustic pressures in the near field of the jet. *Journal of Fluid Mechanics* **813** (1), 716–749.

Schmidt, O. T. & Colonius, T. 2020 Guide to spectral proper orthogonal decomposition. *AIAA Journal* **55** (12), 4013–4041.

Sieber, M., Paschereit, C. O. & Oberleithner, K. 2016 Spectral proper orthogonal decomposition. *Journal of Fluid Mechanics* **792** (1), 798–828.

Tam, C. K.W. & Dong, Z. 1994 Wall boundary conditions for high-order finite-difference schemes in computational aeroacoustics. *Theoretical and Computational Fluid Dynamics* **6** (1), 303–322.

Thurow, B, Samimy, M & Lempert, W 2002 Structure of a supersonic impinging rectangular jet via real-time optical diagnostics. In *32nd AIAA Fluid Dynamics Conference and Exhibit*, pp. 1–12.

Tinney, C. E. & Jordan, P. 2008 The near pressure field of co-axial subsonic jets. *Journal of Fluid Mechanics* **611** (1), 175–204.

Towne, A., Schmidt, O. T. & Colonius, T. 2018 Spectral proper orthogonal decomposition and its relationship to dynamic mode decomposition and resolvent analysis. *Journal of Fluid Mechanics* **847** (1), 821–867.